Editors' Suggestion

Acoustically Induced Giant Synthetic Hall Voltages in Graphene

Pai Zhao,[1] Chithra H. Sharma,[1] Renrong Liang,[2,†] Christian Glasenapp,[1] Lev Mourokh,[3,‡] Vadim M. Kovalev,[4,5,§] Patrick Huber,[1,6] Marta Prada,[7] Lars Tiemann,[1,*] and Robert H. Blick[1]

[1]*Center for Hybrid Nanostructures, Universität Hamburg, Luruper Chaussee 149, 22761 Hamburg, Germany*
[2]*School of Integrated Circuits, Tsinghua University, 100084 Beijing, China*
[3]*Department of Physics, Queens College of the City University of New York, Flushing, New York 11367, USA*
[4]*A.V. Rzhanov Institute of Semiconductor Physics, Siberian Branch of Russian Academy of Sciences, Novosibirsk 630090, Russia*
[5]*Novosibirsk State Technical University, Novosibirsk 630073, Russia*
[6]*Institute of Materials and X-Ray Physics, Hamburg University of Technology, 21073 Hamburg, Germany*
[7]*Institute for Theoretical Physics, Universität Hamburg HARBOR, Building 610 Luruper Chaussee 149, 22761 Hamburg, Germany*

(Received 21 December 2021; revised 8 April 2022; accepted 25 May 2022; published 21 June 2022)

Any departure from graphene's flatness leads to the emergence of artificial gauge fields that act on the motion of the Dirac fermions through an associated pseudomagnetic field. Here, we demonstrate the tunability of strong gauge fields in nonlocal experiments using a large planar graphene sheet that conforms to the deformation of a piezoelectric layer by a surface acoustic wave. The acoustic wave induces a longitudinal and a giant synthetic Hall voltage in the absence of external magnetic fields. The superposition of a synthetic Hall potential and a conventional Hall voltage can annihilate the sample's transverse potential at large external magnetic fields. Surface acoustic waves thus provide a promising and facile avenue for the exploitation of gauge fields in large planar graphene systems.

DOI: 10.1103/PhysRevLett.128.256601

Phonons and their interaction with electrons have a long and rich history in condensed matter physics. Phonons generally exist as random and omnidirectional propagating lattice vibrations that are powered by the finite temperatures in the solid. Surface acoustic waves, henceforth abbreviated as SAW, are very strong directed vibrational modes that propagate predominately along the surface of a piezoelectric crystal. SAW can be launched in a piezoelectric substrate by an interdigitated transducer (IDT) [1], i.e., two interlocking electrodes connected to a frequency generator, which locally "nudges" the piezoelectric substrate to perform a periodic mechanical contraction and expansion. The resulting directed propagation of a mechanical deformation wave along the surface of a substrate has become a heavily exploited technique in sensing applications [2,3] and in basic research of 2D electron systems [4–14] in semiconductor heterostructures.

The interaction between SAW and the quasirelativistic carriers in graphene marries classical and relativistic physics and should significantly revise the acoustic transport of 2D carrier systems. Theory predicts new rich physics, including a crossover from a Schrödinger-like to a Dirac-like behavior that relates to the acoustic wave vector [15]. When graphene is placed on a substrate with passing SAW, the propagating wave drags along carriers in the graphene sheet. Pioneering works have studied the flow of such acoustically induced currents and the buildup of longitudinal voltages under various experimental conditions (temperature, carrier concentration, for different piezoelectric substrates and wiring schemes) [16–20]. Recently, acoustic transport under high magnetic fields and 4.2 Kelvin studied the regime of Landau quantization [21] as many years before in GaAs heterostructures [4,7].

Here, we explore the limits of very high SAW excitation powers in the regime of Dirac physics in a large planar graphene device at cryogenic temperatures. We observe the buildup of a giant longitudinal voltage and a synthetic transverse Hall voltage in the absence of magnetic fields. The acoustically induced synthetic Hall voltage can be exploited to compensate and amplify conventional Hall voltages that arise from classical electrodynamics when carriers are placed in a magnetic field. We argue that SAW-induced strain leads to artificial gauge fields that can account for the generation of the transverse voltage component.

Figure 1 illustrates our sample layout and summarizes the characterization of the graphene layer. A high piezoelectricity of the substrate is key to strongly actuate the graphene by a passing SAW. An optimized hybrid substrate consisting of 900 nm of $LiNbO_3$ that is separated by 2 μm SiO_2 from a p-doped silicon wafer was developed. The p-doped Si acts as a back gate to control carrier type and concentration in the graphene via the gate voltage, V_{BG}. $LiNbO_3$ has a piezoelectric constant 80 times higher than GaAs. The thickness of the dielectric layer is adjusted to the acoustic wavelength and suppresses any leakage of the SAW into the bulk. CVD monolayer graphene (MLG) is transferred to the

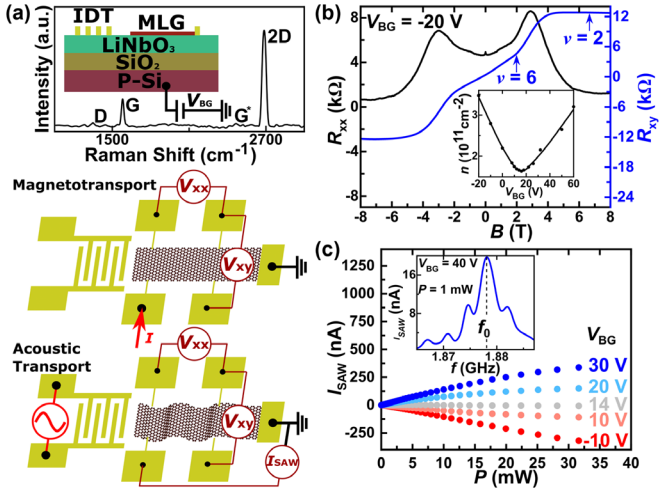

FIG. 1. Device structure, measurement configuration, and characterization. (a) The top main panel shows a Raman spectrum of our CVD monolayer graphene (MLG). The inset is a schematic diagram of the MLG on top of a hybrid LNOI substrate (900 nm of $LiNbO_3$ on 2 μm SiO_2 insulator). The carrier concentration is tuned by a voltage V_{BG} applied to the p-doped substrate. MLG was patterned into a Hall bar of 50 μm width and 400 μm total length (50 μm contact distance). The bottom panels illustrate two measurement configurations. In conventional magnetotransport, a constant current I is passed through the Hall bar. In acoustic transport, a microwave frequency is applied to the IDT (finger width and distance are both 400 nm) and the resulting acoustic current, I_{SAW}, is measured in short-circuited configuration. In both cases, longitudinal and Hall voltages are measured at the same contacts. (b) Exemplary magnetotransport measurement for $V_{BG} = -20$ V. The inset shows the carrier density vs V_{BG}. (c) I_{SAW} as a function of frequency, power, and V_{BG} for the fundamental resonance of the IDT. A measurement for the first harmonic is available in the Supplemental Material [23]. Data were obtained at 4.2 K.

substrate [22] and patterned into a Hall bar close to an IDT (sample details in the caption of Fig. 1). From the Raman spectrum in Fig. 1(a), we deduce a ratio of the 2D/G peaks of 3.5, confirming the presence of a single layer. To abate the amounts of contaminants on the surface, it is thermally annealed inside a vacuum probe at 100 °C for two days prior to cool down to 4.2 K in vacuum. In the following, we will present and discuss data collected from this sample. We reproduced and confirmed the experimental observations on a second sample with different design parameters (see the Supplemental Material [23]).

Conventional magnetotransport was measured with the IDT grounded using a standard lock-in method, schematically illustrated in the lower part of Fig. 1(a) by passing a constant 4 nA (37.3 Hz) alternating current I through a dedicated source contact close to the IDT. A second contact at the opposite end is permanently grounded. In a four-point scheme, we monitor the longitudinal (V_{xx}) and Hall (V_{xy}) voltage with lock-in amplifiers while sweeping the magnetic field, B. The main panel of Fig. 1(b) shows an exemplary measurement of the longitudinal resistance, $R_{xx} = V_{xx}/I$, and Hall resistance, $R_{xy} = V_{xy}/I$, under $V_{BG} = -20$ V, i.e., for a carrier concentration of 3.47×10^{11} cm^{-2} and a mobility $\mu = 6385$ cm^2 V^{-1} s^{-1}. A Hall plateau at Landau level filling factor $\nu = (nh/eB) = 2$ is observed at $B = 6$ T. Detailed magnetotransport measurements are available in the Supplemental Material [23].

We characterized our IDT and the interaction between SAW and graphene as schematically shown in the lower part of Fig. 1(a). A short-circuit configuration is used to enable a steady acoustic current, I_{SAW}. The IDT is driven by an external frequency generator in amplitude modulation mode (modulation depth 100%) for the detection of the induced acoustic currents and voltages by lock-in amplifiers that also provide a reference signal [8]. V_{xx} and V_{xy} are measured at the same contacts as in conventional magnetotransport.

In the following, we will parametrize the SAW strength by the output power of the frequency generator that is given in mW. First, we will concentrate on the acoustic current that is shown in Fig. 1(c). An IDT has a fundamental resonance f_0 that is given by its design parameters. Around f_0, the acoustic wavelength λ matches the finger distance and the piezoelectric substrate resonates. Weaker harmonic resonances, for multiples of λ can also be observed. Our IDT resonates at a fundamental frequency of $f_0 = 1.878$ GHz for which I_{SAW} is at a maximum (Fig. 1(c) inset) at any given SAW power. I_{SAW} is gate-tunable and its sign reflects the carrier type. Measurements in the main panel of Fig. 1(c) demonstrate that I_{SAW} is linear and switches sign when we pass the charge neutrality point (CNP) of our graphene device. The acoustic current density j_{SAW} can be expressed by $j_{SAW} \propto \mu P^* \Gamma v^{-1}$, with P^* being the effective wave intensity, v the wave velocity, and Γ the wave attenuation, all of which are sensitive to the carrier density or, more precisely, the conductivity [14,24]. The sensitivity arises from the interaction of electric fields in the traveling mechanical surface deformation of the $LiNbO_3$ and mobile carriers in the graphene. Our IDT can also operate with the (first) harmonic resonance of $f_1 = 2.872$ GHz that results in weaker acoustic currents but shows a similar dependence on the SAW power (additional data in the Supplemental Material [23]).

A directed net flow of carriers that are subject to scattering will result in a potential difference. Consequently, longitudinal voltages were detected in response to the flow of acoustic currents in graphene [20,25]. With increasing IDT power, we observe that the flow of an acoustic current not only induces the expected longitudinal voltage, V_{xx}, but that also a transverse voltage component, V_{xy}, appears. Figure 2 shows the development of V_{xx} (black) and V_{xy} (blue) with SAW power for the fundamental and first harmonic resonance of the IDT and for three different carrier concentrations at $B = 0$ T. The sign

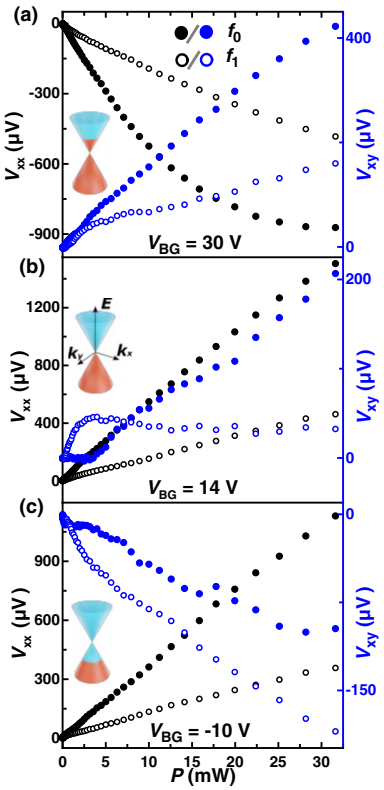

FIG. 2. Acoustically induced voltages as a function of power on the IDT. All measurements are carried out at $B = 0$ T using the "acoustic transport" configuration of Fig. 1(a). Black always represents longitudinal voltages and blue transverse voltages. Closed circles were measured with the fundamental resonance and open circles with the first harmonic of the IDT. From top to bottom are measurements in the electron regime (a), at CNP (b), and in the hole regime (c) of the MLG. Data were obtained at 4.2 K.

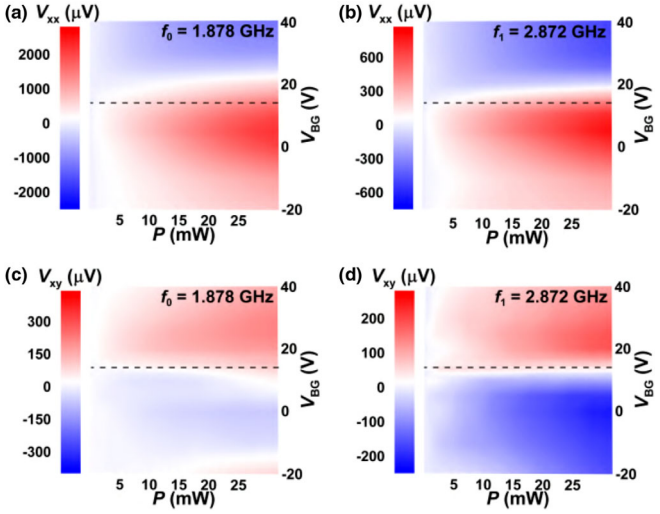

FIG. 3. Acoustically induced voltages measured for different gate voltages and IDT powers. All measurements are performed without external magnetic field at 4.2 Kelvin. (a),(b) Longitudinal voltage for the fundamental and first resonance. (c),(d) Transverse voltage for the fundamental and first resonance. In all plots, the dashed line marks V_{CNP}.

of V_{xx} reflects the dominating carrier type in the graphene layer. It is negative for both IDT resonances when the Fermi energy resides in the conduction band and positive when the Fermi energy lies in the valence band. At the CNP, where I_{SAW} becomes vanishingly small, we still observe a large positive V_{xx} of the order of 1 mV. The CNP in our sample exhibits a broad transition region (Fig. S1(a) in the Supplemental Material [23]) where electrons and holes coexist. With $V_{BG} = 14$ V, holes in the valence band appear to dominate the transport. The relatively large longitudinal voltage component at the CNP is due to the low conductivity of the graphene layer that enables a large phonon pressure, or a small attenuation of the propagating wave, respectively. The existence of the transverse voltage is nonintuitive. It is positive in the electron regime, becomes smaller around the CNP, and then changes sign in the hole regime. The more detailed sampling in Fig. 3 illustrates that the IDT power is the governing force for all carrier regimes.

Prior to discussing the nature of the transverse voltage, we complement our study with an experiment that truly marries classical, quantum, and Dirac physics. At large perpendicular magnetic fields, our device exhibits the quantum Hall effect, with a Hall plateau in the vicinity of 6 T for $V_{BG} = -20$ V [Fig. 1(b)]. We wire our sample again in the conventional magnetotransport configuration and impose an alternating current of $I = 4$ nA. At the same time, we now also fire the IDT at its fundamental resonance that will drive an I_{SAW} and acoustically induce transverse voltage components. Figure 4 shows the total V_{xy} measured vs B (black solid line). The blue line shows the Hall voltage that was measured in the conventional magnetotransport configuration (without SAW) for comparison. We note that while I is constant, I_{SAW} will depend on the magnetic field [21] even for a constant IDT power because the sample conductivity changes when the density of states condenses into Landau levels. By carefully adjusting the IDT power at a constant magnetic field, we are able to completely compensate the conventional Hall voltage by the acoustically induced transverse voltage component. The IDT power that is needed to fully compensate the Hall voltage is not perfectly symmetric for $-B$ and $+B$ as shown in Fig. 4(b) for six exemplary fields. We suppose this to be arising from sample inhomogeneities and the details of the local charge accumulation.

The buildup of a conventional Hall potential is the trivial consequence of the Lorentz force acting on charged carriers. Here, however, we could observe giant quasi-Hall voltages in the absence of an external magnetic field. Below we discuss an intriguing explanation based on gauge fields that arise from the mechanical deformation of the graphene by the SAW.

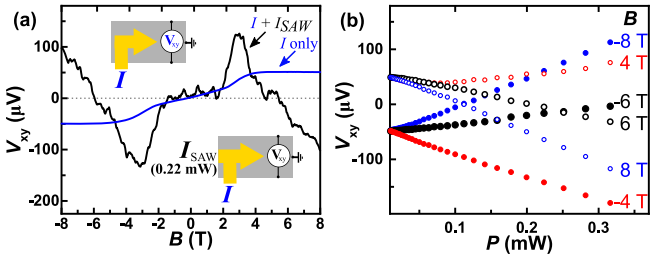

FIG. 4. (a) Ordinary Hall voltage due to a conventional $I = 4$ nA (upper inset and blue solid line) and transverse voltage measured for a superposition of I and I_{SAW} due to $P = 0.22$ mW (lower inset and black solid line). The dotted gray line indicates $V_{\mathrm{xy}} = 0$. (b) Transverse voltage measured for a superposition of I and I_{SAW} at six different B and for varying P. At ± 6 T, $P = 0.2$–0.25 mW is required to fully compensate V_{xy} to zero. Increasing P further will again result in a finite net V_{xy}. Data were obtained at 4.2 K with $V_{\mathrm{BG}} = -20$ V and for an I_{SAW} generated at f_0.

Early during the advent of graphene, it was realized that one of many remarkable consequences of its low-energy Dirac description is the emergence of synthetic gauge fields under lattice deformation [26–28]. Like regular gauge fields that lead to a magnetic flux, synthetic gauge fields affect the carrier dynamics through an effective pseudomagnetic field $\boldsymbol{B} = \boldsymbol{\nabla} \times \boldsymbol{A}$, with $\boldsymbol{A}$ being the vector potential resulting from a distortion of the graphene lattice [29]. Theoretical and experimental work have shown that pseudomagnetic fields can easily exceed tens or even hundreds of Tesla on a nano and micrometer scale by strong local deformation [30–33].

Here, we do not rely on sophisticated nanostructuring. However, the transverse voltage component can be linked to the deformation of the graphene by the SAW and a resulting gauge field [34]. We test this hypothesis by considering a defect-free lattice with the crystallographic axes x_0 and y_0 and a SAW propagation along x, as shown in Fig. 5. The SAW, a piezoelectric surface wave in the $LiNbO_3$ substrate traveling with v_S, is accompanied by propagating piezoelectric fields $\varphi(x, z = 0) = \varphi_0 \cos(kx - \omega t)$

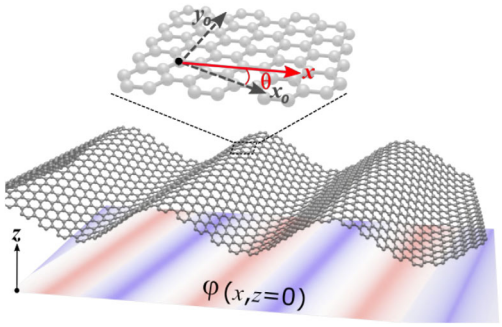

FIG. 5. The piezoelectric potential $\varphi(x, z = 0)$ in the substrate in contact with the deformed graphene. The direction of propagation is $x \| k$ with an arbitrary angle θ with respect to the crystal axes x_0 and y_0.

and a mechanical deformation of the medium that couples or transfers to the graphene layer on its surface at $z = 0$. We are interested in the shear component of the mechanical deformation, $u_y(x, z = 0) = u_0 \cos(kx - \omega t)$, associated with the Bleustein-Gulyaev (BG) SAW. The time dependence of the SAW-induced gauge field has two important consequences: First, in addition to the pseudomagnetic field, there is also the pseudoelectric field, $\boldsymbol{E}^p = -\partial_t \boldsymbol{A}$. Both pseudo fields have opposite signs in nonequivalent valleys K and $-K$ of graphene. Second, all the first-order effects associated with the pseudo fields vanish after the time averaging. However, the second-order effects, such as the appearance of the Hall-like field, survive.

We have derived the corresponding synthetic gauge potential in the Supplemental Material [23]. Here, we will only show the components of the resulting pseudoelectric field, $\boldsymbol{E}^p$, and pseudomagnetic fields, $\boldsymbol{B}^p$, in graphene:

$$\boldsymbol{E}^p = A(t)\omega \begin{pmatrix} \sin(3\theta) \\ \cos(3\theta) \\ 0 \end{pmatrix}, \quad \boldsymbol{B}^p = A(t)k \begin{pmatrix} 0 \\ 0 \\ \cos(3\theta) \end{pmatrix}, \tag{1}$$

with $A(t) = (\beta\Delta/ev_F)(ku_0)\cos(kx - \omega t)$ being a time-dependent prefactor. Here, Δ is the hopping amplitude for electrons in the lattice and β the Gruneisen parameter for acoustic phonons.

The product of nonzero components (second-order effect) enables a Lorentz-like transverse force of the form $F_y \propto \langle E_x^p B_z^p \rangle$, where $\langle \ldots \rangle$ indicates time averaging. The real *piezo*electric field that propagates in the $LiNbO_3$ substrate does not directly contribute to the force on the carriers because it does not change sign in the $-K$ valley. Its product with the pseudomagnetic field vanishes after the summation over the valleys. The product of the pseudoelectric field with the real magnetic field is a first-order effect and also vanishes after time averaging.

We can now provide a semiclassical estimate of the SAW-induced quasi-Hall voltage on the basis of the balance of forces, as given by

$$U_H = \mu \langle E_x^p(t) B_z^p(t) \rangle d = \frac{\mu d}{4} \left(\frac{\beta\Delta}{ev_F} \right)^2 (ku_0)^2 \omega k \sin(6\theta). \tag{2}$$

With our experimental parameters of mobility $\mu = 0.63\ \mathrm{m^2\,V^{-1}\,s^{-1}}$, an assumed SAW amplitude in the $LiNbO_3$ at low temperatures [35,36] $u_0 = 1 \times 10^{-9}$ m, our fundamental resonance frequency $\omega = 2\pi f_0 = 11.7 \times 10^9\ \mathrm{s^{-1}}$, the sample width of $d = 50 \times 10^{-6}$ m, the Gruneisen parameter [33] $\beta \approx 2.5$, the pseudovector potential parameter [33] $(\Delta/ev_F) = 2.5 \times 10^{-6}\ \mathrm{m \cdot T}$, and the wave vector $k = 3 \times 10^6\ \mathrm{m^{-1}}$, we obtain for arbitrary orientations

$$U_H \approx 97\ \mu\mathrm{V} \cdot \sin(6\theta). \quad (3)$$

Our model, based on a balanced (static) force in a perfect crystal, predicts strain-induced synthetic Hall voltages in graphene of the same order that we observed. Below we discuss potential perturbative or spurious parasitic effects in realistic samples that are not captured by this model but which may add to V_{xy}. A full theoretical analysis of the transverse carrier dynamics still needs to be developed.

The measured transverse potential represents a local cross section through the width of our CVD graphene Hall bar and encompasses around 3 or 4 grains [37], which is beneficial. Having only a single grain with θ inadvertently close to 0, 30°,... would suppress U_H. The measured V_{xy} thus represents an average. A complete averaging out to zero, however, would only be possible in the limit of a very high number of grains. Any departure from flatness introduced in the fabrication process also leads to inhomogeneous gauge field contributions [27].

We attribute nonlinearities in $V_{xy}(P)$ around the CNP to the coexistence and fluctuations of electron-hole puddles. These density inhomogeneities smear out and broaden the CNP [see Supplemental Material [23], Fig. S1(a)]. Additional small contributions may arise from spurious reflected attenuated acoustic waves that have bounced off from the edges or the bottom of the substrate. Also, the coupling between substrate and graphene may vary locally.

Contributions from skew scattering will exist but should be insignificantly small. The mean free path is small compared to the sample width. In contrast to the net deflection by a Lorentz force, skew scattering will occur randomly on defects that cannot result in a large charge accumulation.

Despite all these possible spurious contributions, the strong deformation by the SAW appears to dominate and we consistently observe strong acoustic voltages in phase to the currents and only at the IDT resonances. We reproduced these findings on a second sample with different design parameters (data provided in the Supplemental Material [23]) so that the most probable scenario for the observation of synthetic Hall potentials under a SAW is the emergence of gauge fields.

Our study demonstrates that the propagation of a surface acoustic wave in a highly piezoelectric substrate induces large longitudinal and synthetic Hall potentials in a graphene layer that conforms to its surface. The magnitude and sign of the acoustic voltages can be controlled by the carrier concentration and carrier type in the graphene as well as the intensity of the SAW in the supporting substrate. The emergence of the synthetic Hall potential is consistent with gauge fields, induced by the mechanical deformation of the propagating SAW. The observed gauge fields are extremely strong, empowering us to acoustically compensate the conventional Hall voltage that builds up under strong magnetic fields. The high accessibility of these experiments may highlight a new arena for easy and effective control of gauge fields in graphene in fundamental research and applied sciences.

R. H. B. acknowledges support by the Deutsche Forschungsgemeinschaft under Grant No. BL-487/14-1. P. Z. acknowledges financial support by the Zentrum für Hochleistungsmaterialien ZHM, Hamburg, Germany. R. R. L. acknowledges the funding of the National Natural Science Foundation of China (Grant No. 92064002). V. M. K. acknowledges support by the Foundation for the Advancement of Theoretical Physics and Mathematics "BASIS." C. H. S. acknowledges financial support from the Alexander von Humboldt foundation. P. H. acknowledges support by the Deutsche Forschungsgemeinschaft under Grant No. 192346071, SFB 986 "Tailor-Made Multi-Scale Materials Systems," as well as by the Center for Integrated Multiscale Materials Systems CIMMS, funded by Hamburg science authority. All measurements within the scope of this work were performed with *nanomeas* [38].

*Corresponding author.
latieman@physnet.uni-hamburg.de
†liangrr@mail.tsinghua.edu.cn
‡Lev.Murokh@qc.cuny.edu
§vmk111@yandex.ru

[1] R. M. White and F. W. Voltmer, Direct piezoelectric coupling to surface elastic waves, Appl. Phys. Lett. **7**, 314 (1965).
[2] P. Delsing *et al.*, The 2019 surface acoustic waves roadmap, J. Phys. D **52**, 353001 (2019).
[3] S. Okuda, T. Ono, Y. Kanai, T. Ikuta, M. Shimatani, S. Ogawa, K. Maehashi, K. Inoue, and K. Matsumoto, Graphene surface acoustic wave sensor for simultaneous detection of charge and mass, ACS Sensors **3**, 200 (2018).
[4] A. Wixforth, J. P. Kotthaus, and G. Weimann, Quantum Oscillations in the Surface-Acoustic-Wave Attenuation Caused by a Two Dimensional Electron System, Phys. Rev. Lett. **56**, 2104 (1986).
[5] A. Wixforth, J. Scriba, J. P. Kotthaus, G. Weimann, and W. Schlapp, Surface acoustic waves on $GaAs/Al_xGa_{1-x}As$ heterostructures, Phys. Rev. B **40**, 7874 (1989).
[6] A. L. Efros and Y. M. Galperin, Quantization of the Acoustoelectric Current in a Two-Dimensional Electron System in a Strong Magnetic Field, Phys. Rev. Lett. **64**, 1959 (1990).
[7] R. L. Willett, M. A. Paalanen, R. R. Ruel, K. W. West, L. N. Pfeiffer, and D. J. Bishop, Anomalous Sound Propagation at $\nu = 1/2$ in a 2D Electron Gas: Observation of a Spontaneously Broken Translational Symmetry?, Phys. Rev. Lett. **65**, 112 (1990).
[8] A. Esslinger, A. Wixforth, R. W. Winkler, J. P. Kotthaus, H. Nickel, W. Schlapp, and R. Lösch, Acoustoelectric study of localized states in the quantized Hall effect, Solid State Commun. **84**, 939 (1992).
[9] V. I. Falko, S. V. Meshkov, and S. V. Iordanskii, Acoustoelectric drag effect in the two-dimensional electron gas at strong magnetic field, Phys. Rev. B **47**, 9910 (1993).

[10] A. Esslinger, R. W. Winkler, C. Rocke, A. Wixforth, J. P. Kotthaus, H. Nickel, W. Schlapp, and R. Lösch, Ultrasonic approach to the integer and fractional quantum Hall effect, Surf. Sci. **305**, 83 (1994).
[11] J. M. Shilton, D. R. Mace, V. I. Talyanskii, M. Y. Simmons, M. Pepper, A. C. Churchill, and D. A. Ritchie, Experimental study of the acoustoelectric effects in GaAs-AlGaAs heterostructures, J. Phys. Condens. Matter **7**, 7675 (1995).
[12] J. M. Shilton, D. R. Mace, V. I. Talyanskii, M. Y. Simmons, M. Pepper, A. C. Churchill, and D. A. Ritchie, Effect of spatial dispersion on acoustoelectric current in a high-mobility two-dimensional electron gas, Phys. Rev. B **51**, 14770 (1995).
[13] S. H. Simon, Coupling of surface acoustic waves to a two-dimensional electron gas, Phys. Rev. B **54**, 13878 (1996).
[14] M. Rotter, A. Wxiforth, W. Ruile, D. Bernklau, and H. Riechert, Giant acoustoelectric effect in GaAs/$LiNbO_3$ hybrids, Appl. Phys. Lett. **73**, 2128 (1998).
[15] P. Thalmeier, B. Dora, and K. Ziegler, Surface acoustic wave propagation in graphene, Phys. Rev. B **81**, 041409(R) (2010).
[16] V. Miseikis, J. E. Cunningham, K. Saeed, R. ORorke, and A. G. Davies, Acoustically induced current flow in graphene, Appl. Phys. Lett. **100**, 133105 (2012).
[17] L. Bandhu, L. M. Lawton, and G. R. Nash, Macroscopic acoustoelectric charge transport in graphene, Appl. Phys. Lett. **103**, 133101 (2013).
[18] L. Bandhu and G. R. Nash, Controlling the properties of surface acoustic waves using graphene, Nano Res. **9**, 685 (2016).
[19] A. Hernández-Mínguez, Y. T. Liou, and P. V. Santos, Interaction of surface acoustic waves with electronic excitations in graphene, J. Phys. D **51**, 383001 (2018).
[20] J. R. Lane, L. Zhang, M. A. Khasawneh, B. N. Zhou, and E. A. Henriksen, Flip-chip gate-tunable acoustoelectric effect in graphene, J. Appl. Phys. **124**, 194302 (2018).
[21] P. Zhao, L. Tiemann, H. K. Trieu, and R. H. Blick, Acoustically driven Dirac electrons in monolayer graphene, Appl. Phys. Lett. **116**, 103102 (2020).
[22] T. J. Lyon, J. Sichau, A. Dorn, A. Zurutuza, A. Pesquera, A. Centeno, and R. H. Blick, Upscaling high-quality CVD graphene devices to 100 micron-scale and beyond, Appl. Phys. Lett. **110**, 113502 (2017).
[23] See Supplemental Material at http://link.aps.org/supplemental/10.1103/PhysRevLett.128.256601 for detailed sample information, measurement methods, additional measurements of the sample from the main text, measurements of a second sample to verify the observed phenomena and detailed theoretical model.
[24] C. C. Tang, Y. F. Chen, D. C. Ling, C. C. Chi, and J. C. Chen, Ultra-low acoustoelectric attenuation in graphene, J. Appl. Phys. **121**, 12 (2017).
[25] E. Preciado *et al.*, Scalable fabrication of a hybrid field-effect and acousto-electric device by direct growth of monolayer MoS_2/$LiNbO_3$, Nat. Commun. **6**, 8593 (2015).
[26] F. Guinea, M. I. Katsnelson, and M. A. H. Vozmediano, Midgap states and charge inhomogeneities in corrugated graphene, Phys. Rev. B **77**, 075422 (2008).
[27] M. A. H. Vozmediano, M. I. Katsnelson, and F. Guinea, Gauge fields in graphene, Phys. Rep. **496**, 109 (2010).
[28] G. G. Naumis, S. Barraza-Lopez, M. Oliva-Leyva, and H. Terrones, Electronic and optical properties of strained graphene and other strained 2D materials: A review, Rep. Prog. Phys. **80**, 096501 (2017).
[29] F. von Oppen, F. Guinea, and E. Mariani, Synthetic electric fields and phonon damping in carbon nanotubes and graphene, Phys. Rev. B **80**, 075420 (2009).
[30] F. Guinea, M. I. Katsnelson, and A. K. Geim, Energy gaps and a zero-field quantum Hall effect in graphene by strain engineering, Nat. Phys. **6**, 30 (2010).
[31] N. Levy, S. A. Burke, K. L. Meaker, M. Panlasigui, A. Zettl, F. Guinea, A. H. C. Neto, and M. F. Crommie, Strain-induced pseudo-magnetic fields greater than 300 Tesla in graphene nanobubbles, Science **329**, 544 (2010).
[32] S. Z. Zhu, J. A. Stroscio, and T. Li, Programmable Extreme Pseudomagnetic Fields in Graphene by a Uniaxial Stretch, Phys. Rev. Lett. **115**, 245501 (2015).
[33] E. Sela, Y. Bloch, F. von Oppen, and M. B. Shalom, Quantum Hall Response to Time-Dependent Strain Gradients in Graphene, Phys. Rev. Lett. **124**, 026602 (2020).
[34] M. Oliva-Leyva and G. G. Naumis, Sound waves induce Volkov-like states, band structure and collimation effect in graphene, J. Phys. Condens. Matter **28**, 025301 (2016).
[35] R. Shilton, M. K. Tan, L. Y. Yeo, and J. R. Friend, Particle concentration and mixing in microdrops driven by focused surface acoustic waves, J. Appl. Phys. **104**, 014910 (2008).
[36] M. S. Islam and J. Beamish, Piezoelectric creep in $LiNbO_3$, PMN-PT and PZT-5A at low temperatures, J. Appl. Phys. **126**, 204101 (2019).
[37] Graphenea, https://www.graphenea.com/collections/buy-graphene-films/products/monolayer-graphene-on-cu-4-inches (Accessed: 2022-03-03).
[38] *nanomeas*, https://www.nanomeas.com/.